Research Article

Jinlong Xie, Hunan Jiang, Jinyang Li, Fei Huang, Ahsan Zaman, Xingxing Chen, Dan Gao, Yifan Guo*, David Hui, and Zuowan Zhou*

Improved impedance matching by multi-componential metal-hybridized rGO toward high performance of microwave absorption

https://doi.org/10.1515/ntrev-2021-0001
received December 24, 2020; accepted January 7, 2021

Abstract: Microwave-absorbing materials with good microwave absorption performance are of great interest for military applications and human health, which is threatened by electromagnetic radiation pollution. Herein, the design and synthesis of multi-componential metal-hybridized graphene composites via freeze drying and pyrolysis of ferrocene hydrazone complex precursor are reported. Various magnetic nanoparticles are loaded on reduced graphene oxide (rGO) via controlling their pyrolysis temperature. The complex electromagnetic parameters of these hybrids are therefore regulated by the hybrid components. Among them, rGO hybridized by the sea-island-like Fe_2O_3/Fe_3O_4/$FeNi_3$ multi-componential metals shows a good balance of dielectric and magnetic constants. Thus, the improved impedance matching with free space brings about a superior electromagnetic wave absorption performance, especially on the effective absorption bandwidth. The minimum reflection loss (RL) of the hybrids is as low as −40.3 dB at 11 GHz with the RL bandwidth of −10 dB being 4.55 GHz (from 9.25 to 13.8 GHz).

Keywords: microwave absorption, multi-componential metals, reduced graphene oxide

1 Introduction

The rapid growth of modern technologies promotes the applications of electronic devices, providing convenience to human lives or military equipment. However, electronic equipment leads to serious electromagnetic wave pollution [1–5]. Therefore, the development of absorbing materials seems to be necessary. Generally, the microwave absorption (MA) performances of materials are determined by their impedance matching and attenuation behaviors. The former decides the incident electromagnetic wave into the interior of materials that are subsequently consumed by dielectric and magnetic loss as described by the latter [6–9]. But the mismatched dielectric constant and permeability, namely, impedance mismatching that exists in most materials, always lead to a narrow absorbing bandwidth. In this regard, the componential and structural design of materials has aroused the enthusiasm toward good MA performance with broad absorption bandwidth.

Among these research studies, constructing pores in carbon-based materials has been proved to be a meaningful strategy for improving the impedance matching. The air existing in the porous ensures the impedance value of materials close to that of free space. Thus, the porous structure allows a broad absorption bandwidth [10–15]. However, porous materials always possess poor strength [16,17] and are easy to be saturated by adsorbed molecules or clusters due to their high specific surface area [18]. Incorporation of magnetic metal particles with dielectric carbon materials, such as graphene, is another important method for designing absorbing materials. The

* **Corresponding author: Yifan Guo,** Key Laboratory of Advanced Technologies of Materials (Ministry of Education), School of Materials Science and Engineering, Southwest Jiaotong University, Chengdu, 610031, China; Institute of Frontier Science and Technology, Southwest Jiaotong University, Chengdu, 610031, China, e-mail: yfguo@my.swjtu.edu.cn
* **Corresponding author: Zuowan Zhou,** Key Laboratory of Advanced Technologies of Materials (Ministry of Education), School of Materials Science and Engineering, Southwest Jiaotong University, Chengdu, 610031, China; Institute of Frontier Science and Technology, Southwest Jiaotong University, Chengdu, 610031, China, e-mail: zwzhou@swjtu.edu.cn
Jinlong Xie, Hunan Jiang, Jinyang Li, Fei Huang, Ahsan Zaman, Xingxing Chen, Dan Gao: Key Laboratory of Advanced Technologies of Materials (Ministry of Education), School of Materials Science and Engineering, Southwest Jiaotong University, Chengdu, 610031, China
David Hui: Department of Mechanical Engineering, University of New Orleans, New Orleans, LA 70148, United States of America

balanced dielectric constant and permeability achieve a good impedance matching. Graphene layers hybridized with a series of single magnetic metal particles, including Fe, Ni, and their oxides, are synthesized. For example, Co/rGO is simply synthesized by hydrothermal method [19], and Fe-hybridized rGO is achieved through primitive chemical reduction [20]. However, these hybrids exhibit improved but uncontrollable MA performances due to the single component of magnetic particles [21,22]. Subsequently, multi-component metal (McM) compounds are used for constructing graphene-based nanostructures, achieving a tunable MA performance [23,24]. But the limited methods for the componential and structural regulations of McM compounds restrict the development of related graphene nanostructures.

In this work, ferrocene hydrazone condensation bimetallic complex is captured by graphene oxide (GO) sheets. The following freeze drying and pyrolysis of the complex precursor form varieties of magnetic particles depended on the pyrolysis temperature. Compared with the existing methods, pyrolyzing bimetallic precursor is able to achieve a controllable McM@rGO hybrid by simply tuning the annealing temperature. The relationships between their MA performances and structure are systematically studied, which provides a meaningful perspective for the componential and structural design of McM-hybridized graphene toward high MA performances.

2 Experiment

2.1 Materials

GO was synthesized by a modified Hummers method [25]. Nitrilotriacetic acid, hydrazine hydrate, 1,1′-diacetylferrocen, and nickel acetate tetrahydrate were purchased from KeLong Chemistry Company. All the reagents involved in the experiment are analytical reagent without any further purification.

2.2 Synthesis of ferrocene hydrazone condensates

A volume of 100 mL of ethanol was mixed with 100 mL of deionized (DI) water, followed by the addition of nitrilotriacetic acid (3.9 g) and hydrazine hydrate (6 mL). The solution was heated to 85°C and stirred for 0.5 h. Then, 8.1 g of 1,1′-diacetylferrocen was added into the solution together with 10 mL of acetic acid. The mixture was maintained for another 2 h. The separated red precipitate was filtered, washed with ethanol, and then dried at 60°C under vacuum for 12 h to obtain the ferrocene hydrazone condensates (Fc).

2.3 Synthesis of Fc–Ni derivatives

A total of 5.6 g of Fc and 5.6 g of nickel acetate tetrahydrate were added to *N*,*N*-dimethylformamide (150 mL). The mixture was heated to 160°C and kept stirring for 1 h. The precipitate was filtered, washed with ethanol, and then dried at 60°C under vacuum for 12 h to obtain the brown Fc–Ni derivatives.

2.4 Synthesis of multi-componential metal-hybridized rGO

The preparation of McM@rGO is diagrammatically illustrated in Figure S1. In brief, 100 mg of GO was first dissolved in 100 mL of DI water, and the mixture was mildly sonicated (70 W) for 0.5 h to obtain a GO dispersion (1 mg/mL). A total of 180 mg of Fc–Ni derivatives was then added into 20 mL of GO dispersion, followed by the demulsification for 3 min (2,000 rpm) using a demulsified machine. The suspensions were freeze-dried to get the precursors and then annealed at different temperatures for 2 h under the argon atmosphere. The final product was referred to as McM@rGO.

2.5 Characterization

The SEM images were characterized by a field-emission scanning electron microscope (JSM-7001F; JEOL). TEM and high-resolution TEM (HR-TEM) were performed on a transmission electron microscope (Zeiss Libra200). The element distribution was discriminated by the energy-dispersive spectrometer (EDS) mapping (Oxford 8118). XRD patterns were obtained on an X-ray diffractometer (D8 ADVANCE; Bruker) with a Cu Kα radiation (λ = 1.54056 Å). The composition of samples was characterized by the XPS (Escalab Xi$^+$; Thermo Fisher Scientific). Hysteresis loops were tested on a vibrating sample magnetometer (PPMS-9; Quantum Design). The electromagnetic parameters of samples were measured using a vector network analyzer (E5071C, Agilent) in the frequency range of 2–18 GHz. The samples were mixed

with wax with a ratio of 20 wt% and then pressed into cyclic annular with an outer diameter of 7.0 mm and an inner diameter of 3.04 mm for further test.

3 Results and discussion

The annealing process of the precursors always involves the reduction of graphene layers as well as the decomposition of Fc–Ni. The structures of the obtained McM@rGO are significantly dependent on the annealing temperature. Thus, a series of McM@rGO annealed at different temperatures are synthesized to recognize their structural differences. These samples are recorded as McM@rGO-*x*, where *x* refers to the annealing temperatures. The morphologies of the synthesized McM@rGO are first investigated by SEM as depicted in Figure 1. At high temperature, the Fc–Ni attached on the surface of GO decomposes into nanoparticles and annealing temperatures remarkably influence the structures of decomposed particles. It is clear that a higher annealing temperature benefits the uniformity of particle size. But the annealing temperature of 800°C results in submicron particles as shown in Figure 1(c). We notice that an appropriate annealing temperature is important for controlling the particle size. At 600°C, decomposed nanoparticles disperse on the graphene layers uniformly with a size of about 10 nm.

As the annealing process may influence the decomposition of precursors, the XRD patterns of McM@rGO synthesized at different annealing temperatures are tested to recognize their crystalline structures. As shown in Figure 2, the McM@rGO-400 exhibits strong diffraction peaks at 2θ = 30.1, 35.7, 43.1, 57.4, and 62.6°, attributing to the (220), (311), (400), (511), and (440) planes of $NiFe_2O_4$ [26] (Figure S2). Thus, the particles attached on the surface of rGO are supposed to be $NiFe_2O_4$. But the

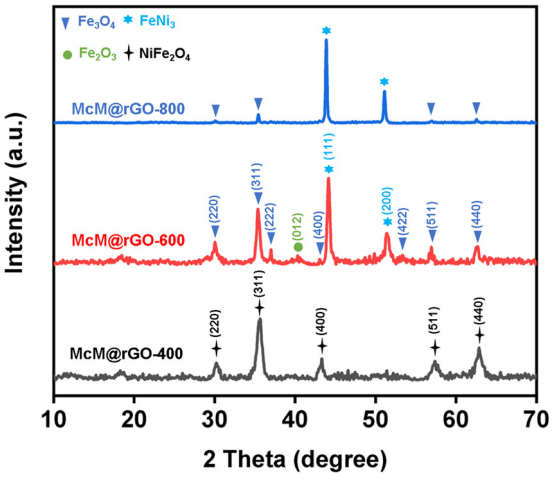

Figure 2: XRD patterns of McM@rGO synthesized at different annealing temperatures.

McM@rGO prepared at 600 and 800°C present different peaks at 2θ = 44.2 and 51.8°, which indicates the generation of $FeNi_3$ [27]. Besides, the (220), (511), and (440) planes of Fe_3O_4, and the (012) plane of Fe_2O_3 are distinguished especially in McM@rGO-600, implying the formation of iron oxides [28,29].

TEM characterizations are applied for further investigations of the nanoparticle-hybridized rGO. As shown in Figure 3(a), $NiFe_2O_4$ densely aggregated on rGO. The particle size of this sample is in the range of 20–100 nm with a wide size distribution. For the McM@rGO annealed at 800°C, the nanoparticles display a narrow size distribution in 40–50 nm. But the TEM image of McM@rGO-600 in Figure 3(b) reveals the uniform distribution of nanoparticles on the surfaces of graphene layers. The size of these particles is about 10 nm, coinciding with the results of SEM characterizations in Figure 1(b). The EDS mapping in Figure S3 identifies the elementary composition of nanoparticles, majorly involving Fe, Ni, and O. This result is in accordance with the XPS as shown in Figure S4. The

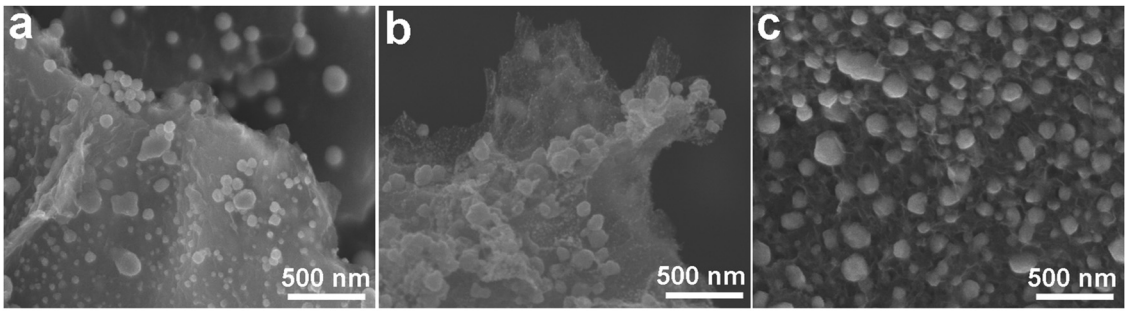

Figure 1: SEM images of McM@rGO synthesized at different annealing temperatures: (a) McM@rGO-400, (b) McM@rGO-600, and (c) McM@rGO-800.

HR-TEM images exhibited in Figure 3(d) clearly demonstrates the multi-componential metals in McM@rGO-600. The well-resolved lattice of 0.364 nm is attributed to the interplanar spacing of (012) in Fe_2O_3 [30]. The particle is surrounded by Fe_3O_4 and $FeNi_3$ as recognized by the marked lattices in the image [31,32]. Thus, the HR-TEM, along with the aforementioned XRD patterns, proves convincing proofs about the multi-componential sea-island structure comprising the island-like Fe_2O_3 nanoparticle as well as the sea-like Fe_3O_4 and $FeNi_3$ alloy as illustrated in Figure 3(e).

Therefore, the structural regulation of McM@rGO is achieved by controlling the annealing temperatures. Fc–Ni attached on the graphene fully transforms into $NiFe_2O_4$ at a relatively low temperature of about 400°C. But with increasing temperature, they are decomposed into Fe_2O_3 nanoparticles with a size of several nanometers. The precursors, meanwhile, are partly reduced by graphene into Fe_3O_4 and $FeNi_3$, forming a continuous phase around the Fe_2O_3 particles. Thus, a coating contrasted by the multi-componential metals is achieved on the rGO layer. With a higher annealing temperature, the precursors are mostly transformed into $FeNi_3$, resulting in the significantly enhanced diffraction peaks as identified in McM@rGO-800.

Considering the intrinsic ferromagnetism of $NiFe_2O_4$, $FeNi_3$ Fe_3O_4, and Fe_2O_3, the magnetic behaviors of McM@rGO hybrids are measured by vibrating sample magnetometer (VSM) at room temperature. The hysteresis loops of these samples are shown in Figure 4. Generally, saturation magnetization and coercivity are regarded as the most important parameters for a magnetic material [33]. As shown in the inset, the magnified curves demonstrate the ferromagnetic of all McM@rGO. Normally, the saturation magnetic intensity is sequenced as follows: Fe_3O_4 [34], $FeNi_3$ [35], $NiFe_2O_4$ [36], and α-Fe_2O_3 [37]. The saturation magnetization (Ms) of McM@rGO-400 is only 18.91 emu/g due to the relatively weak ferromagnetism of $NiFe_2O_4$. But the Ms of McM@rGO-800 is much larger than that of McM@rGO-600, perhaps due to the increased ratio of $FeNi_3$ to Fe_3O_4 as proved by the structural characterization. We notice that McM@rGO-600 possesses the largest remanent magnetization (Mr) and coercivity (Hc) among these samples, which might owe to its refined grains and good dispersion among all samples [38]. Thus, the area enclosed by the hysteresis loop, which represents the magnetic loss capability, is thought to be higher for McM@rGO-600.

The cooperation between dielectric rGO and magnetic McM leads to the changes in complex permittivity

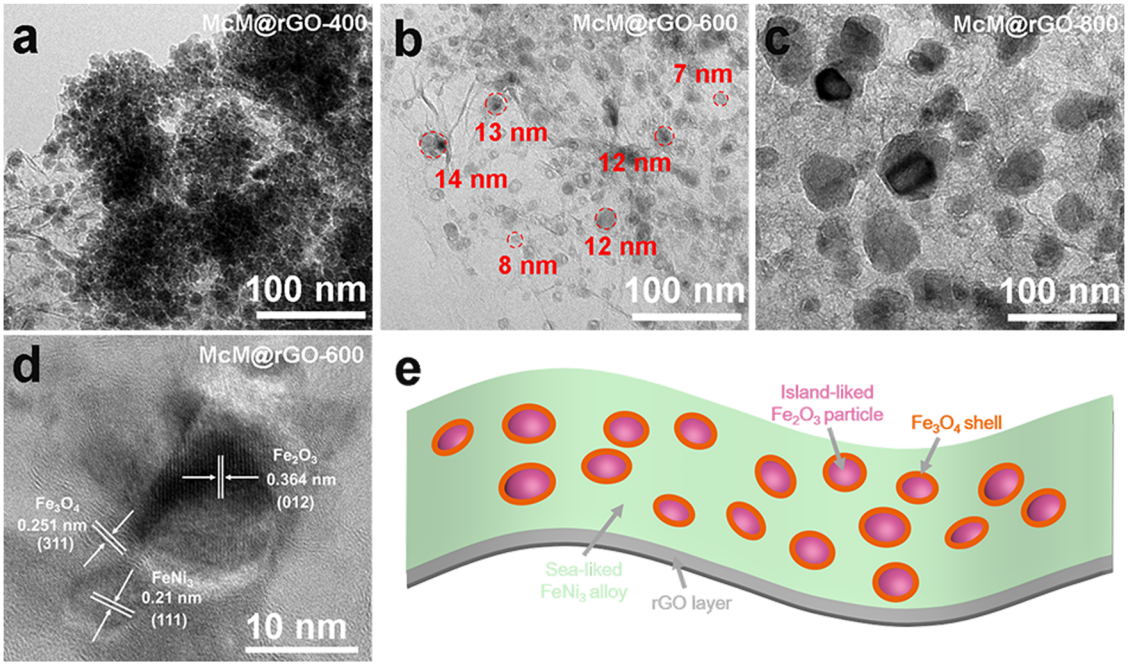

Figure 3: TEM characterizations of McM@rGO synthesized at different temperatures. TEM images of (a) McM@rGO-400, (b) McM@rGO-600, (c) McM@rGO-800, and (d) HR-TEM image of McM@rGO-600. (e) The diagram of the sea-island structure comprised of McMs on the surface of rGO.

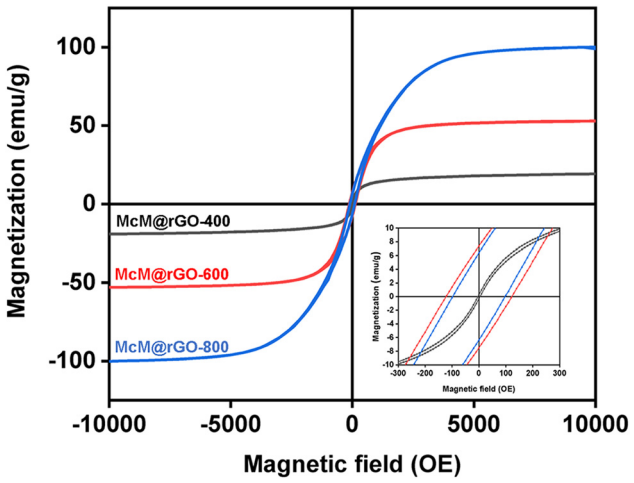

Figure 4: Hysteresis loops of the McM@rGO synthesized at different annealing temperatures. The inset provides an enlarged view of the loops in the range of −300 to 300 OE.

($\varepsilon_r = \varepsilon' - j\varepsilon''$) and permeability ($\mu_r = \mu' - j\mu''$), which is closely related to the MA [39–41]. To investigate the MA performance of the McM@rGO hybrids, frequency-dependent electromagnetic parameters are measured. The real parts of permittivity (ε') and permeability (μ') represent the storage ability of field energy, whereas the imaginary parts of permittivity (ε'') and permeability (μ'') indicate the dissipation capacity [42–45]. The complex permittivities of these synthesized hybrids are given in Figure 5(a and b). Both the real and imaginary parts decrease with an increase in frequency, indicating a frequency dispersion behavior induced by the enhanced polarization lagging in the high frequency [46,47]. The dielectric behaviors of McM@rGO majorly originate from the interfaces between nanoparticles and graphene layers as well as the polarization of residual functional groups [48]. Benefitting from the uniform hybridization between sea-island-like McM and rGO layers, McM@rGO-600 displays an improvement in dielectric dissipation in the range of 9–14 GHz as described by dielectrical dissipation factors ($\tan\delta\varepsilon$) in Figure 5(c). For the situation of complex permeabilities (Figure 5d and e), McM@rGO-400 presents a comparable permeability but few abilities in magnetic loss due to the lossless $NiFe_2O_4$ [49]. The magnetic loss factor ($\tan\delta\mu$) in Figure 5(f) demonstrates a strong magnetic loss in the range of 11–14 GHz, especially for McM@rGO-600. The relative low magnetic loss peak for McM@rGO-800 might be due to the decreased contents of Fe_3O_4 and Fe_2O_3 as proved by XRD patterns.

Reflection loss (RL) is an important index that directly reflects the microwave absorption performance

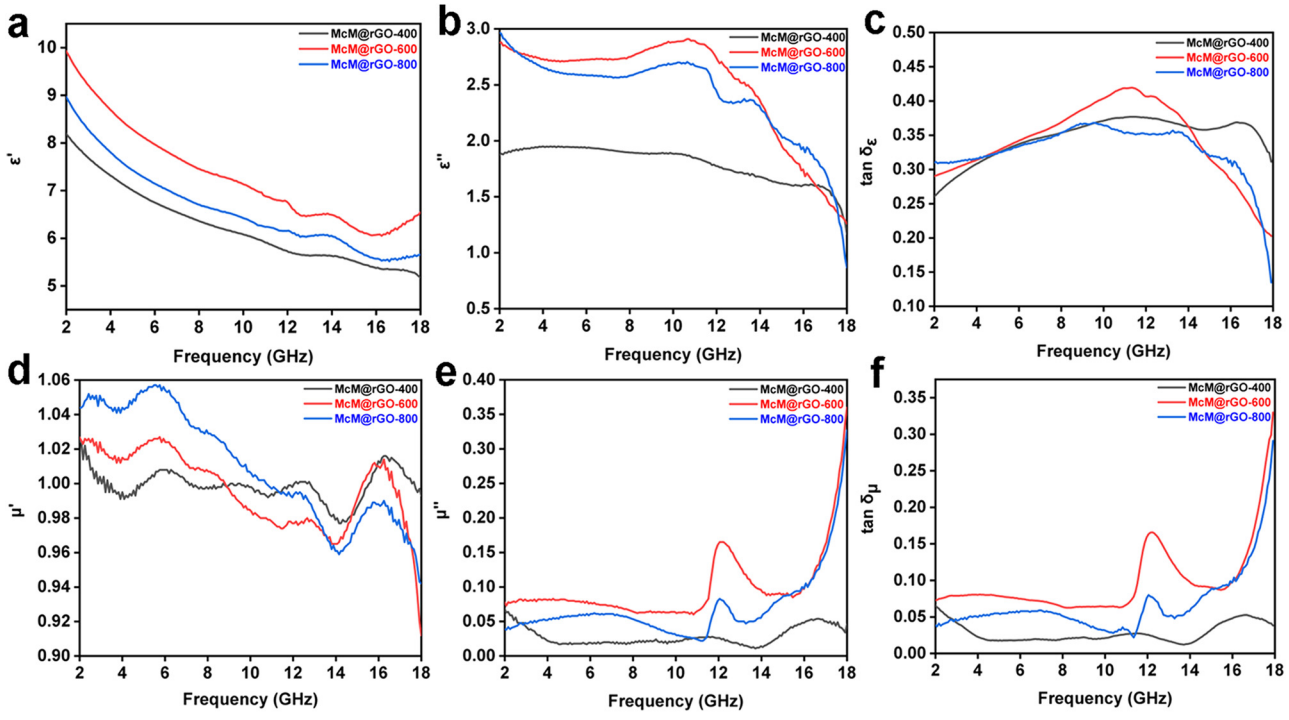

Figure 5: Frequency-dependent electromagnetic parameters of McM@rGO synthesized at different annealing temperatures. (a) ε', (b) ε'', (c) $\tan\delta\varepsilon$, (d) μ', (e) μ'', and (f) $\tan\delta\mu$.

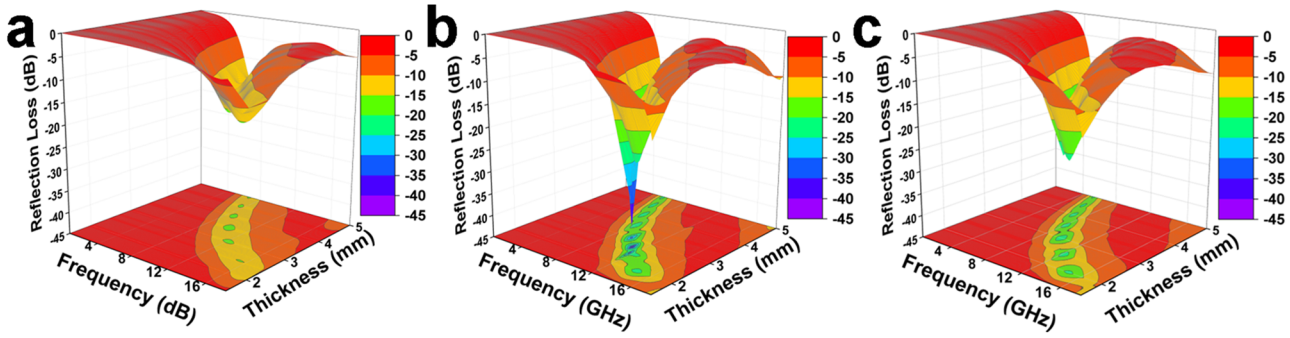

Figure 6: RL curves of McM@rGO at different thicknesses (1.5–5.0 mm) from 2.0 to 18.0 GHz: (a) McM@rGO-400, (b) McM@rGO-600, and (c) McM@rGO-800.

of materials. According to the transmission line theory, the RL is calculated by the following equations (1) and (2) [50,51].

$$\mathrm{RL(dB)} = 20 \log \left| \frac{Z_{\mathrm{in}} - Z_0}{Z_{\mathrm{in}} + Z_0} \right|, \tag{1}$$

$$Z_{\mathrm{in}} = Z_0 \sqrt{\frac{\mu_{\mathrm{r}}}{\varepsilon_{\mathrm{r}}}} \tanh\left(\mathrm{j}\frac{2\pi f d}{c}\sqrt{\mu_{\mathrm{r}}\varepsilon_{\mathrm{r}}}\right), \tag{2}$$

where d, f, and c are the thickness of absorber, frequency of incident microwave, and velocity of light.

In Figure 6(a), McM@rGO-400 demonstrates a weak RL peak, majorly owing to its poor magnetic loss. We notice that the McM@rGO-600 holds a superior MA ability even better than McM@rGO-800. The minimum RL value is down to −40.3 dB at 11 GHz with the effective absorption bandwidth (RL < −10 dB) of 4.55 GHz (from 9.25 to 13.8 GHz) at 2.7 mm. Moreover, the widest effective absorption bandwidth is calculated to be 5.25 GHz with a thickness of only 2.0 mm.

The superior MA performance of McM@rGO-600 is closely related to the improved impedance matching and increased dissipation. The impedance matching values ($|Z_{\mathrm{in}}/Z_0|$) of McM@rGO are derived from electromagnetic parameters and shown in Figure 7. $|Z_{\mathrm{in}}/Z_0|$ illustrates the proximity between the input impedance (Z_{in}) of the absorber and the impedance (Z_0) of the free space. The

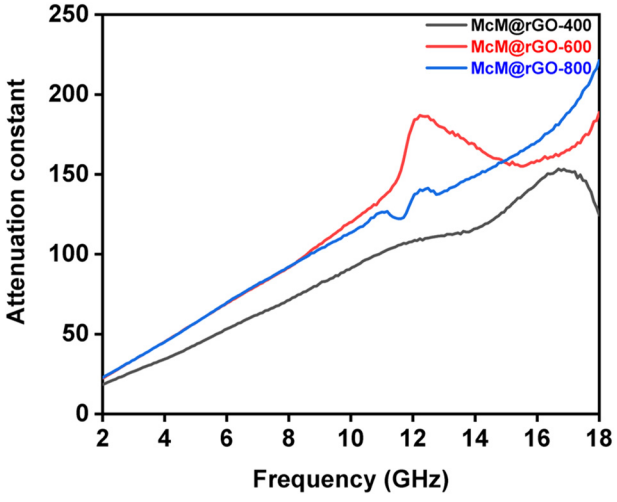

Figure 8: The attenuation constant curves of McM@rGO.

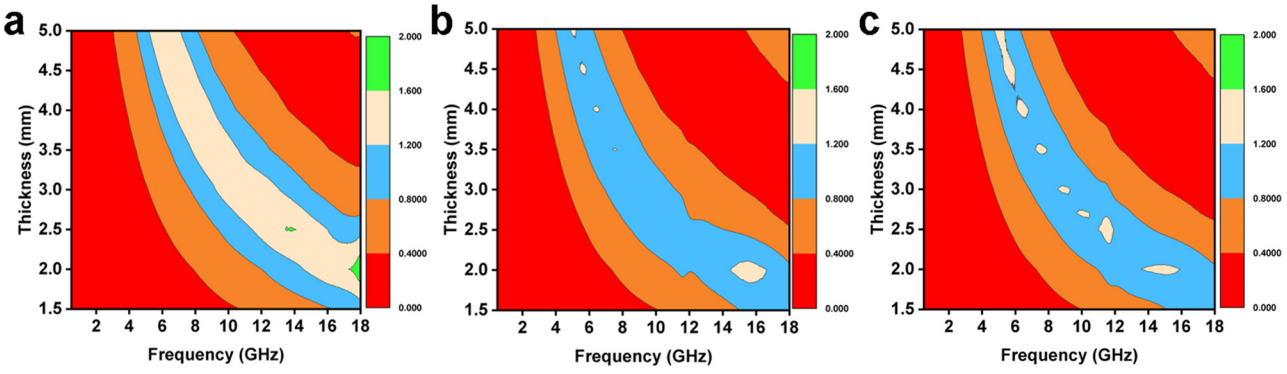

Figure 7: The impedance matching of McM@rGO. $|Z_{\mathrm{in}}/Z_0|$ maps of (a) McM@rGO-400, (b) McM@rGO-600, and (c) McM@rGO-800.

$|Z_{in}/Z_0|$ value of hybrids is expected to be 1 to achieve the maximum incident wave into the interior of the absorber [52]. The blue area represents a good impedance matching (0.8–1.2) as the other colors indicate a mismatching. Benefitting from the matching between permittivity and permeability, McM@rGO-600 possesses the best impedance matching as recognized by the maximum blue area in Figure 7, profiting the incident of microwave for further dissipation.

On the other hand, the attenuation value (α) is used to evaluate the dissipation of incident wave in absorbers [53,54]. The α values of samples are calculated using equation (3), and the results are shown in Figure 8. The increased α, especially in the range of 10–14 GHz for McM@rGO-600, originates from the synergistic enhancements of dielectric and magnetic loss. Moreover, the tiny but uniformly dispersed nanoparticles may also benefit to their MA performance [55].

$$\alpha = \frac{\sqrt{2\pi f}}{c} \times \sqrt{(\mu''\varepsilon'' - \mu'\varepsilon') + \sqrt{(\mu''\varepsilon'' - \mu'\varepsilon')^2 + (\mu'\varepsilon'' - \mu''\varepsilon')^2}}. \quad (3)$$

4 Conclusions

In conclusion, this work achieves the compositional and structural regulations of McM-hybridized rGO by controlling the decomposition and reduction of Fc–Ni precursors. The rGO hybridized by the sea-island-like Fe_2O_3/Fe_3O_4/$FeNi_3$ McM displays a good balance of dielectric and magnetic constants, significantly improving the impedance matching with free space. Therefore, a superior MA performance is realized for the McM@rGO hybrids. The minimum RL of the hybrids is as low as −40.3 dB at 11 GHz with the RL bandwidth of −10 dB being 4.55 GHz (from 9.25 to 13.8 GHz), which seems to be an ideal candidate for high-performance EM wave absorption.

Funding information: The authors gratefully acknowledge the financial support of the National Natural Science Foundation of China (No. 52002338) and the Key R & D Projects in Sichuan Province (No. 2020ZDZX0005 and No. 2020ZDZX0008).

Author contributions: All authors have accepted responsibility for the entire content of this manuscript and approved its submission.

Conflict of interest: The authors state no conflict of interest.

References

[1] Zhang XJ, Zhu JQ, Yin PG, Guo AP, Huang AP, Guo L, et al. Tunable high-performance microwave absorption of $Co_{1-x}S$ hollow spheres constructed by nanosheets within ultralow filler loading. Adv Funct Mater. 2018;28(49):1800761.

[2] Ye F, Song Q, Zhang Z, Li W, Zhang S, Yin X, et al. Direct growth of edge-rich graphene with tunable dielectric properties in porous Si_3N_4 ceramic for broadband high-performance microwave absorption. Adv Funct Mater. 2018;28(17):1707205.

[3] Zhao S, Yan L, Tian X, Liu Y, Chen C, Li Y, et al. Flexible design of gradient multilayer nanofilms coated on carbon nanofibers by atomic layer deposition for enhanced microwave absorption performance. Nano Res. 2018;11(1):530–41.

[4] Wang H, Meng F, Li J, Li T, Chen Z, Luo H, et al. Carbonized design of hierarchical porous carbon/Fe3O4@Fe derived from loofah sponge to achieve tunable high-performance microwave absorption. ACS Sustain Chem Eng. 2018;6(9):11801–10.

[5] Liu Y, Jiang L, Wang H, Wang H, Jiao W, Chen G, et al. A brief review for fluorinated carbon: synthesis, properties and applications. Nanotechnol Rev. 2019;8(1):573–86.

[6] Han M, Yin X, Hou Z, Song C, Li X, Zhang L, et al. Flexible and thermostable graphene/SiC nanowire foam composites with tunable electromagnetic wave absorption properties. ACS Appl Mater Interfaces. 2017;9(13):11803–10.

[7] Zhao B, Guo X, Zhao W, Deng J, Fan B, Shao G, et al. Facile synthesis of yolk-shell Ni@void@SnO_2(Ni_3Sn_2) ternary composites via galvanic replacement/Kirkendall effect and their enhanced microwave absorption properties. Nano Res. 2017;10(1):331–43.

[8] Barathi Dassan EG, Anjang Ab Rahman A, Abidin MSZ, Akil HM. Carbon nanotube-reinforced polymer composite for electromagnetic interference application: a review. Nanotechnol Rev. 2020;9(1):768–88.

[9] Ovid'ko IA. Enhanced mechanical properties of polymer-matrix nanocomposites reinforced by graphene inclusions: a review. Rev Adv Mater Sci. 2013;34(1):19–25.

[10] Cui X, Liang X, Chen J, Gu W, Ji G, Du Y. Customized unique core-shell Fe_2N@N-doped carbon with tunable void space for microwave response. Carbon. 2020;156:49–57.

[11] Wang L, Zhou P, Guo Y, Zhang J, Qiu X, Guan Y, et al. The effect of $ZnCl_2$ activation on microwave absorbing performance in walnut shell-derived nano-porous carbon. Rsc Adv. 2019;9(17):9718–28.

[12] Xu H, Yin X, Li M, Li X, Li X, Dang X, et al. Ultralight cellular foam from cellulose nanofiber/carbon nanotube self-assemblies for ultrabroad-band microwave absorption. ACS Appl Mater Interfaces. 2019;11(25):22628–36.

[13] Zhao H, Yeow Seow JZ, Cheng Y, Xu ZJ, Ji G. Green synthesis of hierarchically porous carbons with tunable dielectric response for microwave absorption. Ceram Int. 2020;46(10):15447–55.

[14] Wu Z, Tian K, Huang T, Hu W, Xie F, Wang J, et al. Hierarchically porous carbons derived from biomasses with excellent

microwave absorption performance. ACS Appl Mater Interfaces. 2018;10(13):11108–15.
[15] Gou G, Meng F, Wang H, Jiang M, Wei W, Zhou Z. Wheat straw-derived magnetic carbon foams: *in situ* preparation and tunable high-performance microwave absorption. Nano Res. 2019;12(6):1423–9.
[16] Liu F, Seo TS. A controllable self-assembly method for large-scale synthesis of graphene sponges and free-standing graphene films. Adv Funct Mater. 2010;20(12):1930–6.
[17] Ovid'ko IA. Mechanical properties of graphene. Rev Adv Mater Sci. 2013;34(1):1–11.
[18] Yang F, Fan X, Wang C, Yang W, Hou L, Xu X, et al. P-doped nanomesh graphene with high-surface-area as an efficient metal-free catalyst for aerobic oxidative coupling of amines. Carbon. 2017;121:443–51.
[19] Zhang C, Wang B, Xiang J, Su C, Mu C, Wen F, et al. Microwave absorption properties of CoS_2 nanocrystals embedded into reduced graphene oxide. ACS Appl Mater Interfaces. 2017;9(34):28868–75.
[20] Li Y, Yu M, Yang P, Fu J. Enhanced microwave absorption property of Fe nanoparticles encapsulated within reduced graphene oxide with different thicknesses. Ind Eng Chem Res. 2017;56(31):8872–9.
[21] Xu W, Wang GS, Yin PG. Designed fabrication of reduced graphene oxides/Ni hybrids for effective electromagnetic absorption and shielding. Carbon. 2018;139:759–67.
[22] Du SM, Chen HY, Hong RY. Preparation and electromagnetic properties characterization of reduced graphene oxide/strontium hexaferrite nanocomposites. Nanotechnol Rev. 2020;9(1):105–14.
[23] Wang Y, Wu X, Zhang W, Luo C, Li J, Wang Q. 3D heterostructure of graphene@Fe_3O_4@WO_3@PANI: preparation and excellent microwave absorption performance. Synth Met. 2017;231:7–14.
[24] Wang L, Huang Y, Sun X, Huang H, Liu P, Zong M, et al. Synthesis and microwave absorption enhancement of graphene@Fe_3O_4@SiO_2@NiO nanosheet hierarchical structures. Nanoscale. 2014;6(6):3157–64.
[25] Zahed M, Parsamehr PS, Tofighy MA, Mohammadi T. Synthesis and functionalization of graphene oxide (GO) for salty water desalination as adsorbent. Chem Eng Res Des. 2018;138:358–65.
[26] Kooti M, Sedeh AN. Synthesis and characterization of $NiFe_2O_4$ magnetic nanoparticles by combustion method. J Mater Sci Technol. 2013;29(1):34–8.
[27] Tahernejad Javazmi F, Shabani Nooshabadi M, Karimi Maleh H. 3D reduced graphene oxide/$FeNi_3$-ionic liquid nanocomposite modified sensor; an electrical synergic effect for development of tert-butylhydroquinone and folic acid sensor. Compos Part B-Eng. 2019;172:666–70.
[28] Moon JY, Jeon YT. Characterization of superlattices of monodisperse Fe_3O_4 nanoparticles in a polystyrene matrix with TEM and XRD. Superlattices Microstruct. 2008;43(2):141–5.
[29] Liu XQ, Tao SW, Shen YS. Preparation and characterization of nanocrystalline alpha-Fe_2O_3 by a sol-gel process. Sens Actuators B-Chem. 1997;40(2–3):161–5.
[30] Wang YL, Li YH, Wang XL, Hou Y, Chen AP, Yang HG. Effects of redox mediators on alpha-Fe_2O_3 exposed by {012} and {104} facets for photocatalytic water oxidation. Appl Catal B-Environ. 2017;206:216–20.
[31] Lv H, Lin L, Zhang X, Gao D, Song Y, Zhou Y, et al. In situ exsolved $FeNi_3$ nanoparticles on nickel doped $Sr_2Fe_{1.5}Mo_{0.5}O_6$ perovskite for efficient electrochemical CO_2 reduction reaction. J Mater Chem A. 2019;7(19):11967–75.
[32] Martínez-Mera I, Espinosa Pesqueira ME, Pérez-Hernández R, Arenas-Alatorre J. Synthesis of magnetite (Fe_3O_4) nanoparticles without surfactants at room temperature. Mater Lett. 2007;61(23–24):4447–51.
[33] Wang J, Cui Y, Wu F, Shah T, Ahmad M, Zhang A, et al. Core-shell structured Fe/Fe_3O_4 @TCNFs@TiO_2 magnetic hybrid nanofibers: preparation and electromagnetic parameters regulation for enhanced microwave absorption. Carbon. 2020;165:275–85.
[34] Han DH, Wang JP, Luo HL. Crystallite size effect on saturation magnetization of fine ferrimagnetic particles. J Magn Magn Mater. 1994;136(1):176–82.
[35] Nasseh N, Taghavi L, Barikbin B, Nasseri MA, Allahresani A. $FeNi_3/SiO_2$ magnetic nanocomposite as an efficient and recyclable heterogeneous fenton-like catalyst for the oxidation of metronidazole in neutral environments: adsorption and degradation studies. Compos Part B Eng. 2019;166:328–40.
[36] Salavati Niasari M, Davar F, Mahmoudi T. A simple route to synthesize nanocrystalline nickel ferrite ($NiFe_2O_4$) in the presence of octanoic acid as a surfactant. Polyhedron. 2009;28(8):1455–8.
[37] Zolghadr S, Kimiagar S, Davarpanah AM. Magnetic property of α-Fe_2O_3–GO nanocomposite. IEEE Trans Magn. 2017;53(12):1–6.
[38] Sun L, Chien CL, Searson PC. Fabrication of nanoporous nickel by electrochemical dealloying. Chem Mater. 2004;16(16):3125–9.
[39] Shu R, Li W, Wu Y, Zhang J, Zhang G. Nitrogen-doped Co-C/MWCNTs nanocomposites derived from bimetallic metal-organic frameworks for electromagnetic wave absorption in the X-band. Chem Eng J. 2019;362:513–24.
[40] Shu R, Zhang G, Wang X, Gao X, Wang M, Gan Y, et al. Fabrication of 3D net-like MWCNTs/$ZnFe_2O_4$ hybrid composites as high-performance electromagnetic wave absorbers. Chem Eng J. 2018;337:242–55.
[41] Shu R, Zhang G, Zhang J, Wang X, Wang M, Gan Y, et al. Fabrication of reduced graphene oxide/multi-walled carbon nanotubes/zinc ferrite hybrid composites as high-performance microwave absorbers. J Alloy Compd. 2018;736:1–11.
[42] Cheng Y, Zhao H, Lv H, Shi T, Ji G, Hou Y. Lightweight and flexible cotton aerogel composites for electromagnetic absorption and shielding applications. Adv Electron Mater. 2020;6(1):1900796.
[43] Wu Y, Shu R, Zhang J, Wan Z, Shi J, Liu Y, et al. Oxygen vacancies regulated microwave absorption properties of reduced graphene oxide/multi-walled carbon nanotubes/cerium oxide ternary nanocomposite. J Alloy Compd. 2020;819:152944.
[44] Agarwal K, Prasad M, Katiyar M, Jaiswal R, Kumar S, Prasad NE. Study of electromagnetic properties of fabricated $NiFe_2O_4$/polyurethane nanocomposites. J Appl Polym Sci. 2020;137(27):48645.
[45] Wang H, Meng F, Huang F, Jing C, Li Y, Wei W, et al. Interface modulating CNTs@PANi hybrids by controlled unzipping of the walls of CNTs to achieve tunable high-performance

microwave absorption. ACS Appl Mater Interfaces. 2019;11(12):12142–53.
[46] Guo Y, Li J, Meng F, Wei W, Yang Q, Li Y, et al. Hybridization-induced polarization of graphene sheets by intercalation-polymerized polyaniline toward high performance of microwave absorption. ACS Appl Mater Interfaces. 2019;11(18):17100–7.
[47] Yang Y, Xia L, Zhang T, Shi B, Huang L, Zhong B, et al. Fe_3O_4@LAS/RGO composites with a multiple transmission-absorption mechanism and enhanced electromagnetic wave absorption performance. Chem Eng J. 2018;352:510–8.
[48] Jia Z, Gao Z, Feng A, Zhang Y, Zhang C, Nie G, et al. Laminated microwave absorbers of A-site cation deficiency perovskite $La0.8FeO_3$ doped at hybrid RGO carbon. Compos Part B Eng. 2019;176:107246.
[49] Wang Y, Gao X, Wu X, Zhang W, Luo C, Liu P. Facile design of 3D hierarchical $NiFe_2O_4$/N-GN/ZnO composite as a high performance electromagnetic wave absorber. Chem Eng J. 2019;375:121942.
[50] Li K, Zhao R, Xia J, Zhao GL. Reinforcing microwave absorption multiwalled carbon nanotube-epoxy composites using glass fibers for multifunctional applications. Adv Eng Mater. 2020;22(3):1900780.
[51] Wu Z, Huang T, Li T, Li L. Facile preparation of a hierarchical C/rGO/FeO_x composite with superior microwave absorption performance. Langmuir. 2019;35(10):3688–93.
[52] Shu R, Wu Y, Li Z, Zhang J, Wan Z, Liu Y, et al. Facile synthesis of cobalt-zinc ferrite microspheres decorated nitrogen-doped multi-walled carbon nanotubes hybrid composites with excellent microwave absorption in the X-band. Compos Sci Technol. 2019;184:107839.
[53] Song WL, Cao MS, Wen B, Hou ZL, Cheng J, Yuan J. Synthesis of zinc oxide particles coated multiwalled carbon nanotubes: dielectric properties, electromagnetic interference shielding and microwave absorption. Mater Res Bull. 2012;47(7):1747–54.
[54] Liu Y, Chen Z, Zhang Y, Feng R, Chen X, Xiong C, et al. Broadband and lightweight microwave absorber constructed by in situ growth of hierarchical $CoFe_2O_4$/reduced graphene oxide porous nanocomposites. ACS Appl Mater Interfaces. 2018;10(16):13860–8.
[55] Wu N, Liu X, Zhao C, Cui C, Xia A. Effects of particle size on the magnetic and microwave absorption properties of carbon-coated nickel nanocapsules. J Alloy Compd. 2016;656:628–34.